Stress corrosion cracking behavior of austenitic stainless steel 316L produced using laser-based powder bed fusion

Ricardo Santamaria, Ke Wang, Mobin Salasi, Mehdi Salem, Philippe Lours, Mariano Iannuzzi, Zakaria Quadir

CORROSION
The Journal of Science and Engineering

Stress corrosion cracking behavior of austenitic stainless steel 316L produced using laser-based powder bed fusion

Journal:	*CORROSION*
Manuscript ID	CJ-2302-OA-4311
Manuscript Type:	Original Article
Date Submitted by the Author:	24-Feb-2023
Complete List of Authors:	Santamaria, Ricardo; Curtin University, Curtin Corrosion Centre Wang, Ke; Curtin University, Salasi, Mobin; Curtin University, Curtin Corrosion Centre Quadir, Zakaria ; Curtin University, Curtin Corrosion Centre Salem, Mehdi ; IMT Mines Albi, Institut Mines-Telecom Lours, Philippe ; IMT Mines Albi, Institut Mines-Telecom Iannuzzi, Mariano; Curtin University
Key Words:	stress corrosion cracking, pitting, residual stress, cracking, stainless steels

Stress corrosion cracking behavior of austenitic stainless steel 316L produced using laser-based powder bed fusion

*Ricardo Santamaria†, * Ke Wang, * Mobin Salasi, * Md Zakaria Quadir, ** Mehdi Salem, *** Philippe Lours, *** and Mariano Iannuzzi **

†ricardo.santamar@postgrad.curtin.edu.au

*Curtin Corrosion Centre, Curtin University, Perth, WA, 6102, Australia.

**John de Laeter Centre, Curtin University, Perth, WA, 6845, Australia.

***IMT Mines Albi, Institut Mines-Telecom, Albi, Tarn, 81013, France.

ABSTRACT

Austenitic stainless steel UNS S31603 (SS316L) is widely used in the resources industry due to its excellent corrosion resistance, ductility, and weldability. Recently, laser-based powder bed fusion (LPBF) manufacturing has gained popularity for creating SS316L components with complex geometries and superior mechanical properties. However, the rapid melting and solidification of the deposited layers during the thermal cycle of LPBF results in residual stresses. Components manufactured through LPBF are frequently used under applied stress in corrosive environments, thus making it crucial to understand their susceptibility to stress corrosion cracking (SCC) and the impact of their residual stresses. This study aimed to investigate the combined effects of applied stress and temperature on the SCC behavior of LPBF SS316L using a series of custom-made C-ring as test specimens. Cold-drawn wrought SS316L was similarly tested for comparison. The outcomes of this study showed that the LPBF SS316L C-rings were highly susceptible to cracking around their printed holes, which was attributed to the residual stresses produced by their printed supports. Therefore, stress relief heat treatment, microhardness test, partial immersion test, and microanalysis techniques such as optical microscopy (OM), scanning electron microscopy (SEM), and electron backscatter diffraction (EBSD), were used to investigate the SCC behavior of the LPBF SS316L C-rings. This study provides valuable insights and lays a foundation for further research into the impact of utilizing C-ring as tests specimens to investigate SCC susceptibility due to the presence of high residual stresses outside the region of interest.

KEY WORDS: *Additive manufacturing, crack initiation, residual stress, SLM, support structure.*

1 INTRODUCTION

Additive manufacturing (AM) is a general term encompassing the technologies that produce physical objects from digital data by adding layers-upon-layers of material.[1-3] When compared to traditional manufacturing, AM has the potential of reducing complexity in the supply chain in terms of quality, impact, cost, speed, and innovation.[4] AM technologies are classified into binder jetting, direct energy deposition, material extrusion, material jetting, sheet lamination, vat photopolymerization, and powder bed fusion (PBF).[2, 3, 5] Nowadays, it is common to use AM to produce engineering grade metals such copper,[6-8] stainless steels,[9-12] titanium-,[13-16] aluminum-,[17-19] and nickel-based alloys.[20-22] Thus, AM technologies have a growing interest from different industries such as biomedical, transport, aerospace, and energy among others.[4, 23-27]

Traditionally manufactured stainless steels such as UNS S31603 (SS316L) are well known for their good corrosion resistance to certain oxidizing environments, formidable ductility, and weldability.[28-31] However, austenitic stainless steels can be susceptible to stress corrosion cracking (SCC) when stressed in tension by the combined action of applied and residual stresses while simultaneously exposed to environments containing halides, e.g., chloride ions.[32-38] SCC is a delayed damage mechanism where the cracks initiate and propagate in the metal at rates

between 10^{-9} to 10^{-6} m/s until the applied stress exceeds the fracture strength of the remaining ligament.[32, 33] Therefore, it is of great interest to employ AM technologies such as PBF to produce SS316L components with better properties than their wrought counterparts.[39-42]

In PBF, an energy source of high intensity, such as a laser (LPBF) or an electron beam (EB) PBF, is employed to melt layers of powdered feedstock that solidify at a calculated rate of ~106 °C/s [43] into near net shape parts. [3, 5, 44] LPBF SS316L can be produced with fully austenitic microstructures,[12, 45, 46] extremely low porosity content,[39, 46, 47] and nano-size non-metallic inclusions. [46, 48, 49] Moreover, LPBF SS316L has shown excellent localized corrosion resistance,[49-51] and outstanding tensile properties. [39, 46, 47] However, the cyclic process of melting and cooling through the deposited layers leaves LPBF SS316L parts with a metastable microstructure containing a high degree of residual stresses. [46, 52, 53] These stresses, which have been reported to be between 250 MPa (36 ksi) and 500 MPa (72 ksi),[46, 52, 54-56] usually start as tension loads at the external surfaces of the component, and gradually turn into compressive loads at its core. [46, 53] Residual stresses can be reduced prior to manufacturing the components, for instance, by optimizing their printing parameters such as laser power, scanning strategy, and printing orientation,[53, 57-60] or by adding post-processing steps to the as-printed object such as stress relief heat treatment,[46, 61-64] or shock peening. [56, 65-67]

This study investigates the impact of residual stresses on the SCC behavior of LPBF-manufactured SS316L using C-rings. To assess this, both stressed and unstressed test specimens were immersed in acidified chloride solution at boiling temperature, and their time-to-crack was monitored. Furthermore, to mitigate the impact of residual stresses on the SCC susceptibility around the printed holes of the LPBF SS316L C-rings, techniques such stress relief heat treatment and partial immersion test were conducted. A detailed post-testing characterization was carried out using optical microscopy (OM), scanning electron microscopy (SEM), and electron backscattered diffraction (EBSD) analysis. The cracking behavior of cold-drawn wrought SS316L C-rings was used as comparison.

2 EXPERIMENTAL PROCEDURES

2.1 Materials

The SS316L used in this investigation was produced using LPBF. The material was additively manufactured utilizing fresh nitrogen-atomized pre-alloyed SS316L powder with an average particle size of 35.7 µm, and a particle size distribution of D_{50} 33.1 µm and D_{90} 55.2 µm. The SS316L powder was kept for at least 12 h in an oven at 50°C (122°F) to remove moisture prior use. Before printing, the built plate was preheated at 100°C (212°F) to decrease thermal gradients, the oxygen content was reduced to less than 0.2%, and the chamber was filled up with high-purity argon. All LPBF SS316L specimens were produced with a layer thickness of 50 µm, no fill contour, no down-skin layer, and using a zig-zag pattern without rotation between layers to achieve the bulk volume. The laser power (P) was 275 W, the scanning speed (V) 700 mm/s, and the hatching space (h) 120 µm. Commercially available cold-drawn wrought SS316L was used to compare the SCC behavior of the LPBF-manufactured SS316L.

LPBF SS316L elemental composition was determined with inductively coupled plasma atomic emission spectroscopy (ICP-AES). Table 1 summarizes the elemental composition of the pre-alloyed SS316L powder used in the LPBF process, and the wrought SS316L cold-drawn rod bar as reported in their manufacture certificates. The Table 1 also shows the externally analyzed composition of the LPBF SS316L, and the nominal composition of UNS S31603 for comparison.

2.2 Microstructure characterization

Phases of the LPBF SS316L and wrought SS316L were identified via X-ray diffraction (XRD) analysis using a Cobalt K alpha powder diffractometer radiation source operating at 35 kV and 40 mA with a LynxEye† detector (Bruker D8 Discover†). The XRD data were collected over

an angular range of 15° to 135°, a step size of 0.015°, and a time interval of 0.7 s. The microscopy analysis was conducted on tested and untested samples that were cut, mounted in cold epoxy resin, wet ground with SiC abrasive paper, and mechanically polished down to 1 µm surface finish. Samples intended for optical microscopy (OM) analysis were chemically etched with a solution containing 10 ml of nitric acid, 100 ml of hydrochloric acid, and 100 ml of deionized water. Samples intended for EBSD analysis were polished to a mirror surface finish with 0.02 µm colloidal silica and then ion-milled for 30 min using a beam voltage of 8 kV at a glancing angle of 4° with full cycle rotational movements (TECHNOORG Linda, SEMPrep2†). All samples for EBSD analysis were surface coated with a 5 µm carbon film to prevent electrostatic charging.

The microstructures were imaged using secondary electron (SE) and backscatter (BS) detectors in a field emission-scanning electron microscope (FE-SEM) (TESCAN system, CLARA†). The crystallographic orientations were mapped using an Oxford† symmetry EBSD detector in the FE-SEM, on samples tilted 70°, with a working distance of 20 mm, a beam energy of 28 kV, and a beam current of 1 nA. A clean-up process was applied to the EBSD data to assimilate any non- or mis-indexed points into the surrounding neighborhood grains, ensuring that less than 10% of the points were modified. Grain boundaries were detected with a threshold misorientation of 10°, a minimum of 8 pixels of fractional difference of misorientation variation, and a kernel size of 3-by-3. Grain size was measured as the maximum Feret diameter. The kernel average misorientation (KAM) maps were obtained using 3-by-3 square kernels and a maximum misorientation angle of 5°. All data acquisition and subsequent post-processing were conducted using the software Aztec† and Aztec Crystal†, respectively.

2.3 Mechanical properties

Mechanical properties, including yield strength (Sy), tensile strength (Su), elongation at fracture, elongation after fracture, reduction of area, and elastic modulus (E), were measured at room temperature. The tests were conducted in triplicate specimens. The LPBF SS316L was tested using custom rectangular specimens that were 55 mm (2.20 in) long, 8 mm (0.30 in) wide, and 2 mm (0.08 in) thick manufactured in the horizontal orientation as shown in the Figure 1a. The displacement during the tensile test was measured using an axial extensometer with a 15 mm (0.60 in) gauge length and +5 mm (0.20 in) travel length (Epsilon TechCorp†). The crosshead speed in the universal testing machine (UTM) was set to 0.225 mm/min within the elastic region, and 0.750 mm/min within the plastic region. The wrought SS316L was tested according to ASTM(1) E8 [68] using rectangular sub-size tensile specimens that were 100 mm (4 in) long, 6 mm (0.24 in) wide, and 3 mm (0.12 in) thick. The specimens were machined from a 25 mm (1 in) diameter rod bar as shown in the Figure 1b. The displacement during the tensile test was measured using an axial extensometer with 25 mm (1 in) gauge length and +25 mm (1 in) travel length (Epsilon TechCorp†). The UTM crosshead speed was set to 0.375 mm/min within the elastic region, and 1.25 mm/min within the plastic region. The Figure 1c shows the geometry and dimensions of the LPBF SS316L and the wrought SS316L tensile specimens.

All tensile tests were conducted using a 50 kN Shimadzu† UTM equipped with 50 kN manual non-shift wedge grips. All data were collected at a rate of 10 Hz using the Trapezium X† software. The actual yield strength (AYS) of the LPBF SS316L and the wrought SS316L were calculated by intersecting their corresponding engineering stress-strain curves with an 0.2% offset line running parallel to the elastic portion of their curves, per ASTM E8. [68] The slope of the offset line, i.e., elastic modulus (E) of the material, was calculated using the least-squared method, per ASTM E111. [69] The microhardness was measured according to ASTM E384 [70] using a microhardness tester (Duramin-4, Struers†), an applied load of 2 Kg (HV2), and a dwell time of 15 s. The bulk density was calculated using the Archimedes principle per standard ASTM B962 [71] with a density kit coupled to an analytical balance with a readability of 0.001 g, and a linearity of ± 0.002 g (ME203, Mettler-Toledo).

† Trade name.
(1) ASTM International, 100 Barr Harbor Dr., West Conshohocken, PA 19428-2959

2.4 Stress corrosion cracking

The SCC behavior was investigated by monitoring the time required by the materials to crack when subjected to a stress corresponding to 60% and 90% of their AYS while immersed in a boiling solution. Unstressed specimens, i.e., 0% AYS, were also tested for comparison. The test solution consisted of 25 wt% NaCl acidified to pH 1.5 with phosphoric acid (H_3PO_4), per ASTM G123. [72] The test specimens utilized in this investigation were C-rings designed per ASTM G38 [73] and shown in the Figure 2a. All tests were carried out at least in duplicates to ensure reproducibility.

The LPBF SS316L C-rings were manufactured in the vertical orientation as shown in the Figure 2a. The supports for the holes were removed by boring them again using a slightly larger drill bit, which also left a surface smoother than the initial as-printed condition. All the C-rings were wet-ground down to 600-grit with SiC abrasive paper, and strained to a constant stress of 60% and 90% AYS, per ASTM G38. [73] The constant-strain assembly shown in the Figure 2b consisted of two PEEK washers, two M6 titanium flat washers, one M6 titanium socket cap bolt, one M6 titanium flanged lock nut, and a strip of clear PTFE heat shrinkable tube molded to the bolt. The stress levels of 60% and 90% AYS were obtained by attaching a 0.3 mm (1/64 in) circumferential strain gauge (FLAB-03-11-1LJC-F, Tokyo Measuring Instruments†) to the convex surface at the middle of the upmost surface of the C-ring's arc and width as shown in the Figure 2b. Then, the bolt was tightened until the reading in the data logger (Almemo 2590, Ahlborn†) indicated the strain value corresponding to the required stress level. All traces of the strain gauges were removed with 600-grit SiC abrasive paper. The electrical insulation between the bolt and the C-ring was verified with a digital multimeter. All the C-rings tested at 0% AYS were also prepared as shown in the Figure 2b, although no stress was applied to the bolt. The cold-drawn wrought SS36L C-rings were similarly prepared and included as control.

Each test condition consisted of a flasks containing 750 ml of test solution and two C-rings, i.e., one from each material stressed to the same corresponding AYS. The ratio of volume of solution per exposed surface area of C-ring was 0.169 mm^3/mm^2. The SCC susceptibility of each material was assessed as the time required to observe the first cracks, i.e., longer exposure times without cracking indicated a lower SCC susceptibility. All C-rings were weekly removed from their test solution, cleaned, and inspected for cracks at a magnification of 20X using OM. C-rings showing SCC were cut and prepared for post-test microscopy analysis. Inversely, C-rings with no cracks continued the test in freshly prepared solution until the next inspection for a maximum of six weeks, per ASTM G123.[72]

The influence of residual stresses on the cracking behavior of LPBF-manufactured SS316L was investigated with two different methods. The first method involved subjecting as-printed duplicate C-rings to heat treatment in a vertical tube furnace under vacuum at 650°C (1200°F) for 2 hours, followed by furnace cooling. After stress relieving, the C-rings were then wet-ground down to 600-grit using SiC abrasive paper, left overnight to recover the passive film, prepared to 0% AYS, and then tested in boiling solution, i.e., approximately 106 °C (223 °F) . In the second method, as-printed duplicate C-rings were stressed to 90% AYS, hung upside-down, and then partially immersed in a boiling solution. The later approach was taken to ensure that the surface under tensile stress, i.e., C-ring's arch, was immersed while the printed holes were kept outside the solution. All C-rings were weekly inspected for cracks.

3 RESULTS

3.1 Microstructure characterization

† Trade name.

Representative XRD spectra of LPBF SS316 and wrought SS316L are shown in the Figure 3. Both materials consisted entirely of γ-austenite (FCC) phase, i.e., no noticeable presence of δ-ferrite (BCC). The Figure 4 shows EBSD maps perpendicular to the build direction and corresponding color-coded inversed pole figures (IPF) of the LPBF SS316L and the wrought SS316L microstructures obtained from untested C-rings. The IPF shows textured LPBF SS316L and wrought SS316L microstructures indicated by the high intensity poles in the {111} pole figure, i.e., 2.32 and 2.27 times random respectively. The Figure 4 also indicates the presence of relatively large austenitic grains in the LPBF SS316L and the wrought SS316L microstructures. Their average grain sizes were 57 ± 52 µm in the LPBF SS316L and 44 ± 34 µm in the wrought SS316L. The overall grain size distributions were D_{50} 39 µm and D_{90} 124 µm for the LPBF SS316L, and D_{50} 34 µm and D_{90} 90 µm for the wrought SS316L. The fitted ellipse aspect ratios were 3.0 ± 1.8 for the LPBF SS316L and 3.9 ± 3.6 for the wrought SS316L.

3.2 Mechanical properties

The Figure 5 shows representative engineering stress-strain curves of the LPBF SS316L and the wrought SS316L, along with their corresponding 60% and 90% AYS. As shown in the figure, LPBF SS316L behaved in a ductile manner similarly to its wrought counterpart, i.e., an initial linear portion of elastic deformation followed by a non-linear portion of plastic deformation with similar degree of strain hardening. The mechanical properties of the LPBF SS316L were slightly lower than the properties of the wrought SS316L. The Sy, Su, and the elongation at fracture of the LPBF SS316L were 529 MPa (77 ksi), 656 MPa (95 ksi), and 43%, while for the wrought SS316L they were 646 MPa (94 ksi), 717 MPa (104 ksi), and 49%. The wrought SS316L had a bulk density of 7.953 ± 0.027 g/cm^3, while the LPBF had a slightly lower value of 7.894 ± 0.013 g/cm^3, which corresponded to a porosity of less than 1%. The mechanical properties of both materials are summarized in Table 2. The average microhardness of the as-printed LBPF SS316L, the heat-treated LBPF SS316L, and the wrought SS316L were 224 ± 3 HV2, 195 ± 2 HV2, and 282 ± 3 HV2, respectively.

3.3 Stress corrosion cracking

Evidence of SCC in the as-printed LPBF SS316L C-rings tested in boiling solution while stressed to 0% and 90% AYS is shown in the Figures 6a and 6b, respectively. The figures show that, regardless of the applied stress, both stressed and unstressed C-rings cracked from corrosion pits located at the edges of their printed holes. In addition to this, the Figure 7 shows a FE-SEM image of highly branched SCC that initiated at the printed hole on an unstressed LPBF SS316L C-ring. Moreover, the Figure 8 shows the transgranular nature of the SCC in the LPBF SS316L. The SCC behavior of as-printed LPBF SS316L C-rings under different applied stress levels while fully immersed boiling solution is summarized in the Table 3. It was also observed that fully immersed as-printed LPBF C-rings took longer to crack when higher stress levels were applied. However, the cracks kept initiating from the printed holes, regardless of the applied load.

It was hypothesized that the continuous cracking from the printed holes of the LPBF 316L C-ring was caused by residual stress around them, which accelerated the pitting nucleation and subsequent SCC. The effect of residual stresses on the SCC of LPBF SS316L was investigated in this study by heat-treating as-printed C-rings. The Figure 9 shows KAM maps perpendicular to the build direction of the as-printed and heat-treated LPBF SS316L C-rings. The as-printed LPBF SS316L microstructure contains local strain around their grain boundaries caused by its processing history. This local strain, depicted by the green areas in the Figure 9a, indicates a high degree of residual stresses. [74, 75] Inversely, the microstructure of the heat-treated LBPBF SS316L shows less areas with local strain as depicted in the Figure 9b. A quantitative representation of the reduction in residual stresses due to the heat treatment is shown in the Figure 9c. It can be seen from this figure that the magnitude of the KAM angles were reduced due to the stress relief effect of the heat treatment procedure. The overall KAM distributions went from D_{50} 0.96°, D_{90} 1.89° in the as-printed LPBF SS316L, to D_{50} 0.64°, D_{90} 1.43° in the heat-treated LPBF SS316L. Furthermore, the Figure 10a shows the SCC of the heat-treated LPBF SS316L C-ring when tested in boiling solution without an applied stress, i.e., 0% AYS. In addition, the Figures 10b and 10c show that the SCC also originated from

the printed hole and propagated transgranularly through the microstructure. These findings indicate that, when heat-treated, the LPBF SS316L unstressed C-rings improved their SCC resistance by cracking after 15 days, i.e., one more week than the as-printed C-rings. However, the cracks kept originating from the printed holes, regardless of the stress-relieving procedure.

The as-printed LPBF SS316L C-rings stressed to 90% AYS were partially immersed as shown in the Figure 11. In this test condition, i.e., 25% NaCl solution with pH 1.5 at boiling temperature, the oxygen concentration in the solution would be much lower than the concentration at room temperature. [76] This suggests that the pitting and the SCC were caused by hydrogen reduction reaction rather than oxygen reduction reaction. Therefore, both partial and fully immersion tests should produce similar results. The findings from the partial immersion test showed that the SCC occurred at the upmost convex region of LPBF 316L C-ring, i.e., where the applied stress is maximum. [73, 77] This SCC behavior can be seen in the Figure 12a along with the behavior of its fully immersed wrought counterpart shown in the Figure 12b. Moreover, it can be seen from the Figure 12b, that the SCC in the wrought SS316L C-ring was perpendicular to the direction of the applied stress. This figure also shows that the cracking originated from one of the cut edges of the wrought SS316L C-ring. The reason for this may be attributed to the residual stresses introduced during the machining process conducted to fabricate the wrought specimens from the rod bar, which potentially affected the SCC resistance of the material. [35, 38, 78]

SCC was observed at the area of maximum applied stress in the partially immersed LPBF SS316L C-rings after two weeks,, i.e., one extra week compared to its fully immersed wrought counterpart. The cracks in both materials exhibited similar SCC behavior, including transgranular cracking and crack branching as shown in the Figure 13. Furthermore, after visual inspection, no cracks were observed around the printed holes of the LPBF SS316L C-rings. In this study, the impact of residual stresses on the SCC resistance of the 3D printed material was observed. However, the use of C-rings with printed holes in fully immersing tests was not an appropriate method for evaluating the SCC susceptibility of LPBF SS316L.

4 DISCUSSION

The results of this study demonstrated that both the as-printed and heat-treated LPBF SS316L C-rings were prone to SCC near the printed holes when exposed to boiling acidified chloride solution as depicted in the Figures 6, 7, 8 and 10. However, when partially immersed and tested under stress, the as-printed LPBF C-rings had a similar SCC behavior than their wrought counterparts such as: i) cracking at the area of highest applied stress rather than at their printed holes, ii) transgranular cracking, and iii) crack branching as shown in the Figures 12 and 13. These outcomes highlight previously reported influence of residual stresses on the behavior of SCC in austenitic stainless steel. [79]

The findings of this study were consistent with the established understanding that stress relief heat treatment in LPBF components can enhance their SCC resistance by reducing residual stress. [46, 61-64, 80] This was demonstrated by the extended time it took for the 0% AYS heat-treated LPBF C-rings to crack compared to the as-printed counterparts when tested in boiling solution, see Table 3. Nevertheless, like in the as-printed C-rings, the cracks in their heat-treated counterparts initiated at the edges of the printed holes as depicted in the Figures 6 and 10a. This suggests that the stress relief process was not entirely effective, which was supported by the fact that the heat-treated C-rings had a microhardness only 13% lower than that of the as-printed ones.

The test conducted on the LPBF-manufactured C-rings revealed the presence of corrosion pits over their convex surfaces, particularly around the edges of their printed holes but especially at the support/hole interface. These areas are characterized by the presence of highly localized tensile residual stresses [52], suggesting that, due to the presence of corrosion pits they may have contributed to the increased SCC

susceptibility around the printed holes. It is noteworthy that the cracks propagated perpendicularly to the print direction of the C-rings as illustrated in Figures 6 and 10a. A clock-like diagram in the Figure 14a shows that the cracks originated at identical sites, specifically the 3 and 9 o'clock positions, which were located 90° away from the support/hole interface. These observations provide further evidence of the role of residual stresses in the development of SCC in LPBF-manufactured components.

It was hypnotized that the ends of the supports connected to the printed holes of the C-rings, which are located at 12 and 6 o'clock positions as depicted in Figure 14b, underwent volumetric contraction as a consequence of the rapid cooling from the melting temperatures during the production of the LPBF SS316L C-rings. [3, 5, 44] Consequently, a compressive stress effect was introduced through the supporting structure which resulted in the formation of two additional sites of maximum tensile residual stress located at the 3 and 9 o'clock positions, as shown in the Figure 14b. This stress effect, resembling of a "C-ring within the C-ring" scenario, is believed to be the primary cause of the continuous cracking of the C-rings at the 3 and 9 o'clock positions.

This study also found that the SCC susceptibility of the LPBF C-rings decreased as the applied stress increased as given in Table 3. This was particularly observed in the unstressed LPBF C-rings, which exhibited faster cracking than their stressed counterparts. However, this unexpected result could be explained using a vector analysis. The Figure 14c shows that when a C-ring is not under stress, the highest tensile residual stress is present at the 9 o'clock position. However, when the C-ring is subjected to a stress such as 60% or 90% AYS, the stress acts perpendicular to the main component of the residual stress, thus leading to a reduction in magnitude and a chance in direction. This "relieving" effect is hypothesized to have reduced the impact of the residual stress around the printed holes. Nevertheless, the fact that all stressed LPBF C-rings kept cracking at their printed holes, suggests that the resulting stress in this area remained to be significantly higher than the one externally applied.

The results from the partial immersion tests, as reported in Table 3, indicated that the LPBF C-rings developed SCC after two weeks at the upmost point of the arch as shown in the Figure 12a. Moreover, no cracks were observed at the printed holes, thus confirming the absence of any residual stress influencing the SCC of the material. This improved SCC resistance could be attributed to a delay in pitting nucleation or a crack arrest effect caused by its microstructure, although further analysis is necessary, including testing LPBF C-rings manufactured at different orientations with drilled holes instead of printed ones.

5 CONCLUSIONS

The present study aimed to investigate the SCC behavior of LPBF-manufactured SS316L through the examination of stressed and unstressed C-rings after being tested in acidified chloride solution at boiling temperature. The study included a stress relief heat treatment and a partial immersion test to mitigate the effect of residual stresses, as well as a comprehensive microstructure characterization to analyze the cracking behavior at the tested conditions. Based on the findings of this investigation, the following conclusions can be drawn:

- The residual stresses inherent to the LPBF process and their complex distribution introduced by the printed supports have a marked adverse effect on the SCC resistance of LPBF SS316L C-rings. This observation has far-reaching implications as it highlights the potential for residual stress to exist in printed parts which will result in a decreased SCC resistance.

- It is important to exercise caution when using C-rings as test specimens for investigating the SCC susceptibility of LBPF-manufactured SS316L, due to the significant influence of residual stresses. Further assessments should be considered to determine the optimal printing parameters, such as print orientation or print supports, to minimize the presence of residual stresses.

- Evidence was provided suggesting that the LPBF SS316L may demonstrate greater resistance to SCC compared to its cold-drawn counterpart, provided that the effect of residual stresses is mitigated or insulated. This was demonstrated through a partial immersion test, which showed that the absence of residual stresses resulted in the LPBF C-rings taking an extra week to crack due to smaller corrosion pits delaying the nucleation of cracks.

- While the results indicate that a stress relief heat treatment may enhance the SCC resistance of the LPBF SS316L, further research is necessary to establish the extent of improvement that can be achieved and to determine the optimal temperature and duration of the process.

6 ACKNOWLEDGMENTS

The authors acknowledge the financial support of Woodside Energy, as well as the access to the instruments of the Microscopy and Microanalysis Facility (MMF) at Curtin University, and the LPBF SS316L manufactured C-rings supplied by the IMT Mines Albi, Institut Mines-Telecom in France.

7 REFERENCES

1. "Additive manufacturing — General principles — Terminology" (CH-1211 Geneva 20: ISO, 2015).
2. L. Yang, K. Hsu, B. Baughman, D. Godfrey, F. Medina, M. Menon, S. Wiener, *Additive manufacturing of metals: the technology, materials, design and production*, Springer, 2017).
3. B. Redwood, F. Schöffer, B. Garret, *The 3D printing handbook: technologies, design and applications*, (Amsterdam: 3D Hubs B.V, 2017).
4. M. Attaran, *Business Horizons* 60, 5 (2017): p. 677-688.
5. "Additive Manufacturing - General Principles - Part 2: Overview of process categories and feedstock" (CH-1211 Geneva 20: ISO International, 2015).
6. S.D. Jadhav, L.R. Goossens, Y. Kinds, B. Van Hooreweder, K. Vanmeensel, *Additive Manufacturing* 42 (2021): p. 101990.
7. H. Miyanaji, D. Ma, M.A. Atwater, K.A. Darling, V.H. Hammond, C.B. Williams, *Additive Manufacturing* 32 (2020): p. 100960.
8. J. Huang, X. Yan, C. Chang, Y. Xie, W. Ma, R. Huang, R. Zhao, S. Li, M. Liu, H. Liao, *Surface and Coatings Technology* 395 (2020): p. 125936.
9. R. Santamaria, M. Salasi, S. Bakhtiari, G. Leadbeater, M. Iannuzzi, M.Z. Quadir, *Journal of Materials Science* (2022): p. 1-17.
10. D. Karlsson, C.-Y. Chou, N.H. Pettersson, T. Helander, P. Harlin, M. Sahlberg, G. Lindwall, J. Odqvist, U. Jansson, *Additive Manufacturing* 36 (2020): p. 101580.
11. J.W. Elmer, J. Vaja, J.S. Carpenter, D.R. Coughlin, M.J. Dvornak, P. Hochanadel, P. Gurung, A. Johnson, G. Gibbs, *Welding Journal* 99, LLNL-JRNL-771645; LA-UR-19-23147 (2020):
12. E. Liverani, S. Toschi, L. Ceschini, A. Fortunato, *Journal of Materials Processing Technology* 249 (2017): p. 255-263.
13. Z. Lin, K. Song, X. Yu, *Journal of Manufacturing Processes* 70 (2021): p. 24-45.
14. B. Dutta, F.S. Froes, *Metal powder report* 72, 2 (2017): p. 96-106.
15. D. Zhang, D. Qiu, M.A. Gibson, Y. Zheng, H.L. Fraser, D.H. StJohn, M.A. Easton, *Nature* 576, 7785 (2019): p. 91-95.
16. M.Y. Mendoza, P. Samimi, D.A. Brice, B.W. Martin, M.R. Rolchigo, R. LeSar, P.C. Collins, *Metallurgical and Materials Transactions A* 48, 7 (2017): p. 3594-3605.
17. N.T. Aboulkhair, M. Simonelli, L. Parry, I. Ashcroft, C. Tuck, R. Hague, *Progress in materials science* 106 (2019): p. 100578.
18. E. Louvis, P. Fox, C.J. Sutcliffe, *Journal of Materials Processing Technology* 211, 2 (2011): p. 275-284.
19. L. Pantělejev, D. Koutný, D. Paloušek, J. Kaiser, "Mechanical and microstructural properties of 2618 Al-Alloy processed by SLM remelting strategy," Materials science forumTrans Tech Publ, 2017), p. 343-349.
20. C.Y. Yap, H.K. Tan, Z. Du, C.K. Chua, Z. Dong, *Rapid Prototyping Journal* (2017):
21. L.N. Carter, C. Martin, P.J. Withers, M.M. Attallah, *Journal of Alloys and Compounds* 615 (2014): p. 338-347.
22. E. Martin, A. Natarajan, S. Kottilingam, R. Batmaz, *Additive Manufacturing* 39 (2021): p. 101894.
23. S.C. Altıparmak, B. Xiao, *Journal of Manufacturing Processes* 68 (2021): p. 728-738.
24. A.J. Pinkerton, *Optics & Laser Technology* 78 (2016): p. 25-32.

25. C. Fredriksson, *Procedia manufacturing* 33 (2019): p. 139-144.
26. A.J. Sheoran, H. Kumar, P.K. Arora, G. Moona, *Procedia Manufacturing* 51 (2020): p. 663-670.
27. T.D. Ngo, A. Kashani, G. Imbalzano, K.T. Nguyen, D. Hui, *Composites Part B: Engineering* 143 (2018): p. 172-196.
28. P. Marshall, *Austenitic stainless steels: microstructure and mechanical properties*, Springer Science & Business Media, 1984).
29. A. Di Schino, in *Manufacturing and applications of stainless steels*, ed., vol. 10 MDPI, 2020), p. 327.
30. A. Outokumpu Stainless, *Avesta Resarch Centre, Avesta, Sweden* (2013):
31. M.F. McGuire, *Stainless Steel for Design Engineers*, (Materials Park, OH: ASM INternational, 2008).
32. R.C. Newman, in *Corrosion Mechanisms in Theory and Practice*, CRC Press, 2011), p. 511-556.
33. R.H. Jones, *Stress-Corrosion Cracking: Materials Performance and Evaluation*, ed., R.H. Jones, ASM International, 2017).
34. H.J. Russell, *Stress Corrosion Cracking*, (Materials Park, Ohio: ASM International, 1992).
35. W. Zhang, K. Fang, Y. Hu, S. Wang, X. Wang, *Corrosion Science* 108 (2016): p. 173-184.
36. S. Ghosh, (2012):
37. S.G. Acharyya, A. Khandelwal, V. Kain, A. Kumar, I. Samajdar, *Materials Characterization* 72 (2012): p. 68-76.
38. S. Wang, Y. Hu, K. Fang, W. Zhang, X. Wang, *Corrosion Science* 126 (2017): p. 104-120.
39. J. Suryawanshi, K.G. Prashanth, U. Ramamurty, *Materials Science and Engineering: A* 696 (2017): p. 113-121.
40. R. Casati, J. Lemke, M. Vedani, *Journal of Materials Science & Technology* 32, 8 (2016): p. 738-744.
41. Y.n. Song, Q. Sun, K. Guo, X. Wang, J. Liu, J. Sun, *Materials Science and Engineering: A* 793 (2020): p. 139879.
42. T. Ronneberg, C.M. Davies, P.A. Hooper, *Materials & Design* 189 (2020): p. 108481.
43. T. DebRoy, H.L. Wei, J.S. Zuback, T. Mukherjee, J.W. Elmer, J.O. Milewski, A.M. Beese, A. Wilson-Heid, A. De, W. Zhang, *Progress in Materials Science* 92 (2018): p. 112-224.
44. L. Bian, N. Shamsaei, J.M. Usher, *Laser-based additive manufacturing of metal parts: modeling, optimization, and control of mechanical properties*, CRC Press, 2017).
45. A. Woźniak, M. Adamiak, G. Chladek, J. Kasperski, *Archives of Metallurgy and Materials* 65 (2020):
46. Q. Chao, S. Thomas, N. Birbilis, P. Cizek, P.D. Hodgson, D. Fabijanic, *Materials Science and Engineering: A* 821 (2021): p. 141611.
47. T. Kurzynowski, K. Gruber, W. Stopyra, B. Kuźnicka, E. Chlebus, *Materials Science and Engineering A* 718 (2018): p. 64-73.
48. V.B. Vukkum, J. Christudasjustus, A.A. Darwish, S.M. Storck, R.K. Gupta, *npj Materials Degradation* 6, 1 (2022): p. 2.
49. C. Man, C. Dong, T. Liu, D. Kong, D. Wang, X. Li, *Applied Surface Science* 467-468 (2019): p. 193-205.
50. M.H. Shaeri Karimi, M. Yeganeh, S.R. Alavi Zaree, M. Eskandari, *Optics & Laser Technology* 138 (2021): p. 106918.
51. G. Sander, S. Thomas, V. Cruz, M. Jurg, N. Birbilis, X. Gao, M. Brameld, C.R. Hutchinson, *Journal of The Electrochemical Society* 164, 6 (2017): p. C250-C257.
52. P. Dong, F. Vecchiato, Z. Yang, P.A. Hooper, M.R. Wenman, *Additive Manufacturing* 40 (2021): p. 101902.
53. P. Bian, J. Shi, Y. Liu, Y. Xie, *Optics & Laser Technology* 132 (2020): p. 106477.
54. R.J. Williams, F. Vecchiato, J. Kelleher, M.R. Wenman, P.A. Hooper, C.M. Davies, *Journal of Manufacturing Processes* 57 (2020): p. 641-653.
55. A.S. Wu, D.W. Brown, M. Kumar, G.F. Gallegos, W.E. King, *Metallurgical and Materials Transactions A* 45, 13 (2014): p. 6260-6270.
56. N. Alharbi, *The International Journal of Advanced Manufacturing Technology* 119, 3 (2022): p. 2285-2299.
57. J. Hajnys, M. Pagáč, J. Měsíček, J. Petru, M. Król, *Materials* 13, 7 (2020): p. 1659.
58. X. Yan, J. Pang, Y. Jing, *Materials* 12, 17 (2019): p. 2719.
59. E. Malekipour, H. El-Mounayri, "Scanning Strategies in the PBF Process: A Critical Review," ASME International Mechanical Engineering Congress and ExpositionAmerican Society of Mechanical Engineers, 2020), p. V02AT02A055.
60. P. Pant, *Residual stress distributions in additively manufactured parts: effect of build orientation*, vol. 1869, Linköping University Electronic Press, 2020).
61. M. Kumaran, V. Senthilkumar, T. Sathies, C.T. Justus Panicker, *Materials Letters* 313 (2022): p. 131766.
62. M. Kamariah, W. Harun, N. Khalil, F. Ahmad, M. Ismail, S. Sharif, "Effect of heat treatment on mechanical properties and microstructure of selective laser melting 316L stainless steel," IOP Conference Series: Materials Science and EngineeringIOP Publishing, 2017), p. 012021.
63. K. Burdová, H. Jirková, L. Kučerová, I. Zetková, J. Mach, *Manufacturing Technology* 22, 3 (2022): p. 261-266.
64. S. Leuders, T. Lieneke, S. Lammers, T. Tröster, T. Niendorf, *Journal of Materials Research* 29, 17 (2014): p. 1911-1919.
65. T. Gundgire, T. Jokiaho, S. Santa-aho, T. Rautio, A. Järvenpää, M. Vippola, *Materials Characterization* 191 (2022): p. 112162.
66. N. Kalentics, E. Boillat, P. Peyre, C. Gorny, C. Kenel, C. Leinenbach, J. Jhabvala, R.E. Logé, *Materials & Design* 130 (2017): p. 350-356.
67. N. Kalentics, E. Boillat, P. Peyre, S. Ćirić-Kostić, N. Bogojević, R.E. Logé, *Additive Manufacturing* 16 (2017): p. 90-97.
68. "Standard Test Methods for Tension Testing of Metallic Materials" (West Conshohocken, PA: ASTM International, 2016).
69. "Standard Test Method for Young's Modulus, Tangent Modulus, and Chord Modulus" (West Conshohocken, PA: ASTM International, 2017).
70. "Standard Test Method for Microindentation Hardness of Materials" (West Conshohocken, PA: ASTM International, 2017).
71. "Standard Test Methods for Density of Compacted or Sintered Powder Metallurgy (PM) Products Using Archimedes' Principle" (West Conshohocken, PA: ASTM International, 2017).
72. "Standard test method for evaluationg stress-corrosion cracking of stainless steel alloys with different nickel content in boiling acidified sodium chloride solution" (West Conshohocken, PA: ASTM International, 2015).
73. "Standard practice for making and using C-ring stress-corrosion test specimens" (West Conshohocken, PA: ASTM International, 2013).
74. M. Tong, X. Di, C. Li, D. Wang, *Materials Characterization* 144 (2018): p. 631-640.
75. M. Calcagnotto, D. Ponge, E. Demir, D. Raabe, *Materials Science and Engineering: A* 527, 10-11 (2010): p. 2738-2746.
76. W. Xing, M. Yin, Q. Lv, Y. Hu, C. Liu, J. Zhang, in *Rotating Electrode Methods and Oxygen Reduction Electrocatalysts*, eds. W. Xing, G. Yin , J. Zhang, (Amsterdam: Elsevier, 2014), p. 1-31.

77. S. Huzni, M. Ridha, A.K. Ariffin, "Stress Distribution Analysis on Four Types of Stress Corrosion Cracking Specimen," Key Engineering MaterialsTrans Tech Publ, 2011), p. 194-199.
78. D.Y. Jang, T.R. Watkins, K.J. Kozaczek, C.R. Hubbard, O.B. Cavin, *Wear* 194, 1 (1996): p. 168-173.
79. D. Spencer, M. Edwards, M. Wenman, C. Tsitsios, G. Scatigno, P. Chard-Tuckey, *Corrosion Science* 88 (2014): p. 76-88.
80. J.L. Bartlett, X. Li, *Additive Manufacturing* 27 (2019): p. 131-149.
81. "Standard Specification for Stainless Steel Bars and Shapes" (West Conshohocken, PA: ASTM International, 2015).
82. H.M. Ledbetter, *Journal of Applied Physics* 52, 3 (1981): p. 1587-1589.
83. "Standard Terminology Relating to Corrosion and Corrosion Testing" (West Conshohocken, PA 19428-2959 USA: ASTM International, 2010).

8 FIGURE CAPTIONS

FIGURE 1. a) Horizontal printing orientation of the LPBF-manufactured SS316L rectangular specimens, b) schematics of the wrought SS316L specimens machined from a 25 mm (1 in) diameter cold-drawn rod bar, and c) drawings showing the geometry and dimensions in mm of the rectangular specimens used for tensile testing LPBF SS316L (top) and wrought SS316L (bottom).

FIGURE 2. Custom C-ring specimen used to investigate the SCC susceptibility of LPBF SS316L and wrought SS316L. a) Drawings and dimensions in mm, and b) schematics of the constant-strain assembly according to ASTM G38.

FIGURE 3. XRD spectra of LPBF SS316L and wrought SS316L showing the presence of γ (FCC) austenite as the only phase in their microstructures.

FIGURE 4. a) EBSD map and corresponding color-coded inverse pole figures with respect to the Z axis of as-printed LPBF SS316L, and b) cold-drawn wrought SS316L untested C-rings showing textured microstructures.

FIGURE 5. Engineering stress-strain curves of LPBF SS316L and wrought SS316L along with the location of their corresponding 60% and 90% AYS.

FIGURE 6. a) SCC in the as-printed LPBF SS316L unstressed C-ring when tested in boiling solution, and b) SCC in the as-printed LPBF SS316L C-ring tested in boiling solution while stressed at 90% AYS.

FIGURE 7. FE-SEM image showing SCC in unstressed as-printed LPBF SS316L C-ring that initiated from its printed hole and propagated perpendicular to the print direction. The highlighted blue region in the depicted C-ring shows the location of the crack.

FIGURE 8. Band contrast image and corresponding EBSD map of SCC in as-printed unstressed LPBF SS316L C-ring tested in boiling solution. It can be seen that the crack is transgranular. The highlighted blue region in the depicted C-ring shows the location of the crack.

FIGURE 9. a) KAM map of untested as-printed LPBF SS316L C-ring showing a microstructure populated with residual stresses represented by the local plastic deformation depicted by the green areas. b) KAM map of untested heat-treated LPBF SS316L showing a reduction of the residual stresses. c) KAM histogram showing the redistribution of local misorientations after heat treatment of the LBPF SS316L.

FIGURE 10. SCC in heat-treated LPBF SS316L unstressed C-ring when tested in boiling solution shown in a) photographic image, b) EBSD map and, c) KAMP map.

FIGURE 11. Test schematics of the as-printed LPBF SS316L C-ring stressed to 90% AYS and partially immersed in boiling solution.

FIGURE 12. C-rings showing SCC at their areas of maximum applied stress, i.e., 90% AYS, when tested in boiling solution. a) As-printed LPBF SS316L partially immersed, and b) wrought SS316L completely immersed.

FIGURE 13. Etched microstructures showing transgranular SCC in a) as-printed LPBF SS316L C-rings partially immersed in boiling solution while stressed at 90% AYS, and b) wrought SS316L C-ring fully immersed in boiling solution while stressed at 90% AYS.

FIGURE 14. a) Depiction of the residual stresses produced in the hole/support interface of the C-rings, b) depiction of an unstressed C-ring with SCC initiating from corrosion pits at the 3 and 9 o'clock sites, and c) depiction of a stressed C-ring and the "relieving" effect of the applied load over the residual stresses.

9 TABLES

TABLE 1: Elemental composition of the pre-alloyed SS316L powder, LPBF-manufactured SS316L, wrought SS316L cold-drawn rod bar, and nominal composition of UNS S31603

Chemical composition in wt%										
Material	**Source**	**Fe**	**C**	**Cr**	**Ni**	**Mo**	**Si**	**Mn**	**P**	**S**
Powder SS316L	Material certificate	Bal.	0.01	17.7	12.6	2.36	0.65	0.90	0.007	0.01
LPBF SS316L	ICP-AES analysis	Bal.	0.02	17.5	12.3	2.02	0.06	0.62	<0.01	0.01
Wrought SS316L	Material certificate	Bal.	0.02	16.7	10.1	2.03	0.04	1.72	0.024	0.02
UNS S31603	ASTM A276 [81]	Bal.	Max. 0.03	16.0 – 18.0	10.0 – 14.0	2.00 – 3.00	Max. 1.00	Max. 2.00	Max. 0.045	Max. 0.03

TABLE 2. Mechanical properties of the as-printed LPBF SS316L, wrought SS316L, and standard requirements for UNS S31603

Material	**Elastic Modulus (E)**	**Yield Strength (Sy)**	**Tensile Strength (Su)**	**Elongation at fracture**	**Elongation after fracture**	**Reduction of area**	**Bulk density**
	GPa (ksi)	MPa (ksi)	MPa (ksi)	%	%	%	g/cm^3
LPBF SS316L	211 ± 12 (30.6 ± 1.7)10^3	529 ± 4 (77 ± 0.6)	656 ± 7 (95 ± 1.0)	43 ± 1	12 ± 2	45 ± 1	7.894 ± 0.013
Wrought SS316L	214 ± 7 (31.0 ± 1.0)10^3	646 ± 8 (96 ± 1.2)	717 ± 6 (104 ± 0.9)	49 ± 5	13 ± 2	66 ± 2	7.953 ± 0.027
UNS S31603 [81]	202 [82] (29.3)10^3	Min. 170 (25)	Min. 485 (70)	Min. 40	n/a	Min. 40	7.98 [83]

TABLE 3. SCC behavior of the LPBF SS316L and the wrought SS316L C-rings tested at different conditions in acidified chloride boiling solution. The number in the cells corresponded to the week when the cracks were observed. Hyphens correspond to untested conditions.

Stainless steel 316L C-rings in boiling solution				
	Partially immersed	**Fully immersed**		
Stress level	LPBF As-printed	Wrought Cold-drawn	LPBF As-printed	LPBF Heat-treated
0% AYS	-	3	1	2
60% AYS	-	2	2	-
90% AYS	2	1	3	-
Crack location	Arch	Arch	Hole	Hole

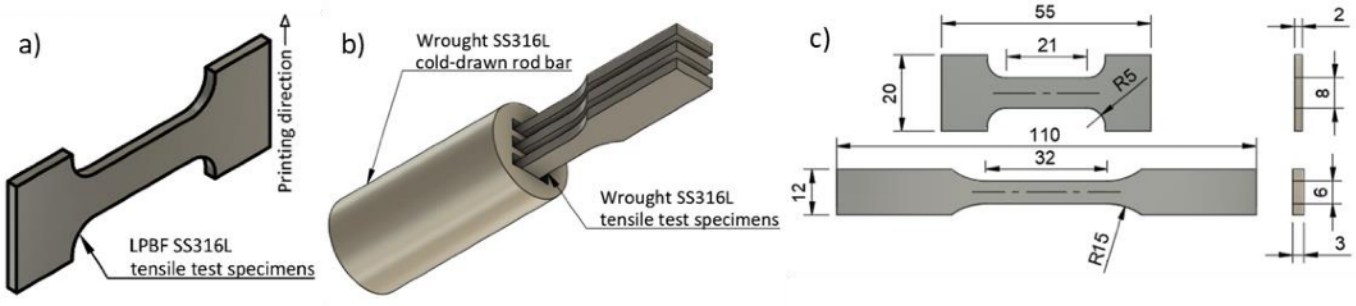

FIGURE 1. a) Horizontal printing orientation of the LPBF-manufactured SS316L rectangular specimens, b) schematics of the wrought SS316L specimens machined from a 25 mm (1 in) diameter cold-drawn rod bar, and c) drawings showing the geometry and dimensions in mm of the rectangular specimens used for tensile testing LPBF SS316L (top) and wrought SS316L (bottom).

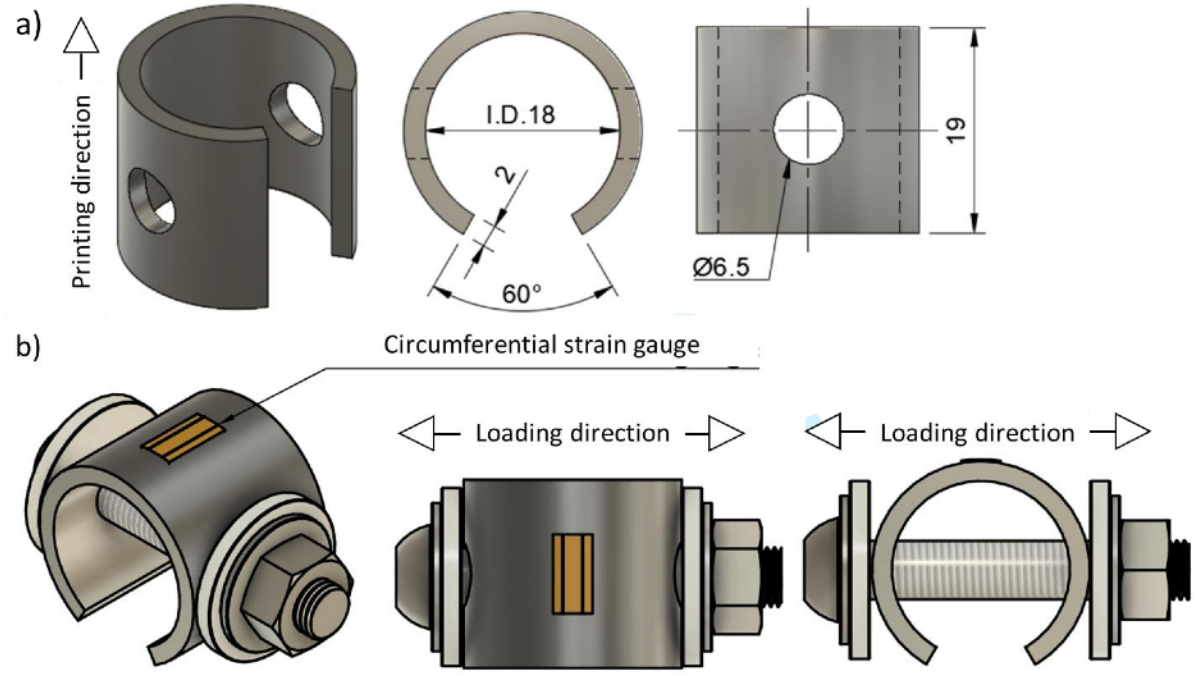

FIGURE 2. Custom C-ring specimen used to investigate the SCC susceptibility of LPBF SS316L and wrought SS316L. a) Drawings and dimensions in mm, and b) schematics of the constant-strain assembly according to ASTM G38.

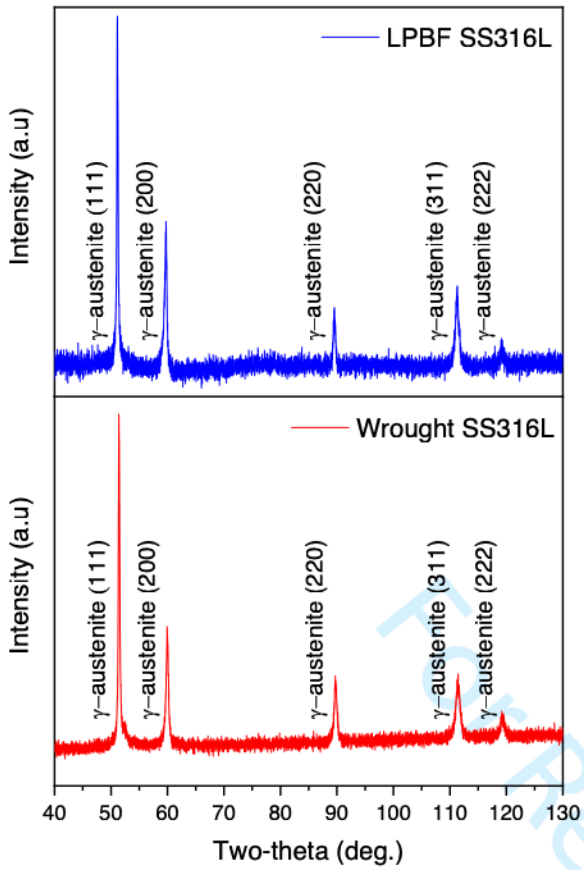

FIGURE 3. XRD spectra of LPBF SS316L and wrought SS316L showing the presence of γ (FCC) austenite as the only phase in their microstructures.

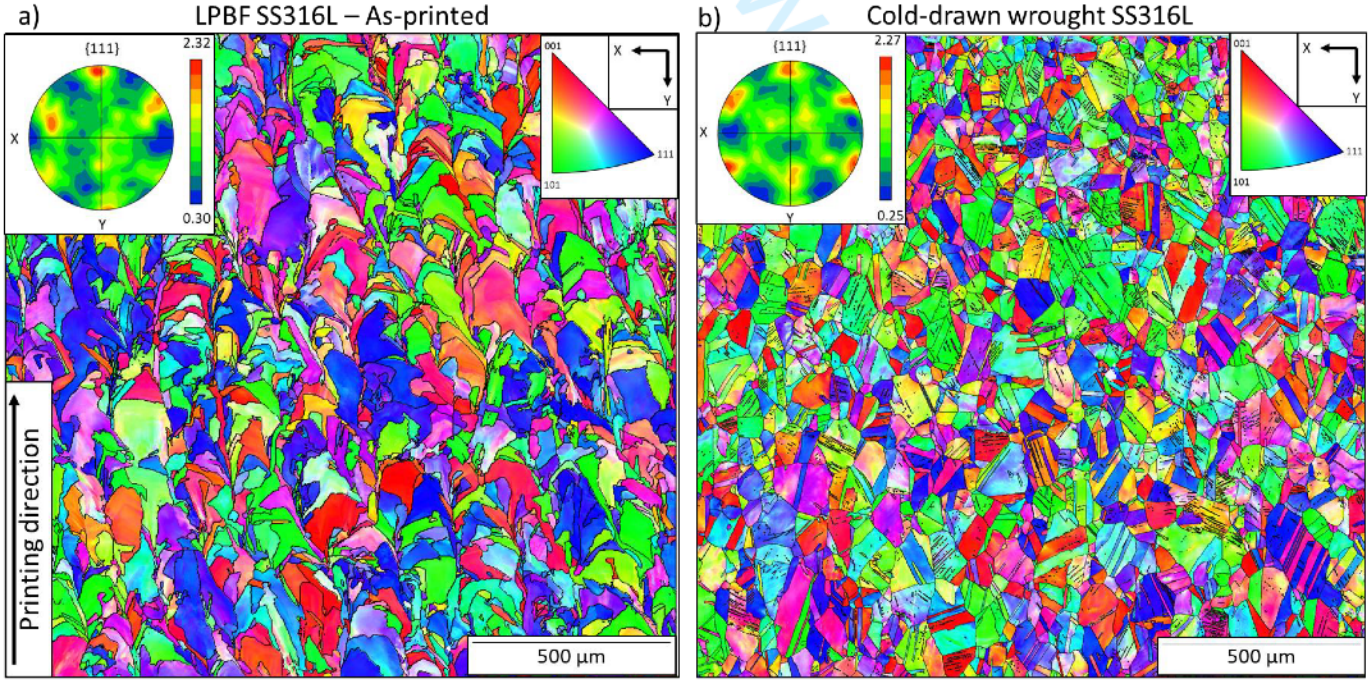

FIGURE 4. a) EBSD map and corresponding color-coded inverse pole figures with respect to the Z axis of as-printed LPBF SS316L, and b) cold-drawn wrought SS316L untested C-rings showing textured microstructures.

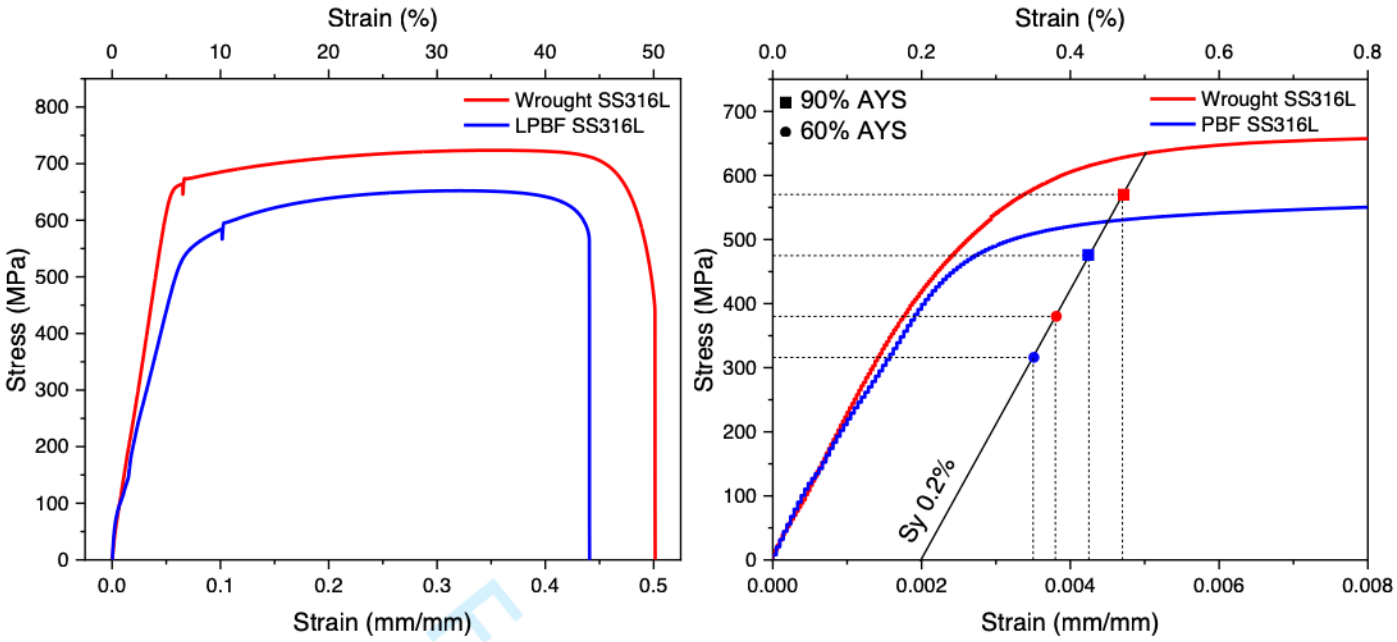

FIGURE 5. Engineering stress-strain curves of LPBF SS316L and wrought SS316L along with the location of their corresponding 60% and 90% AYS.

a) As-printed LPBF SS316L, 0% AYS, boiling solution

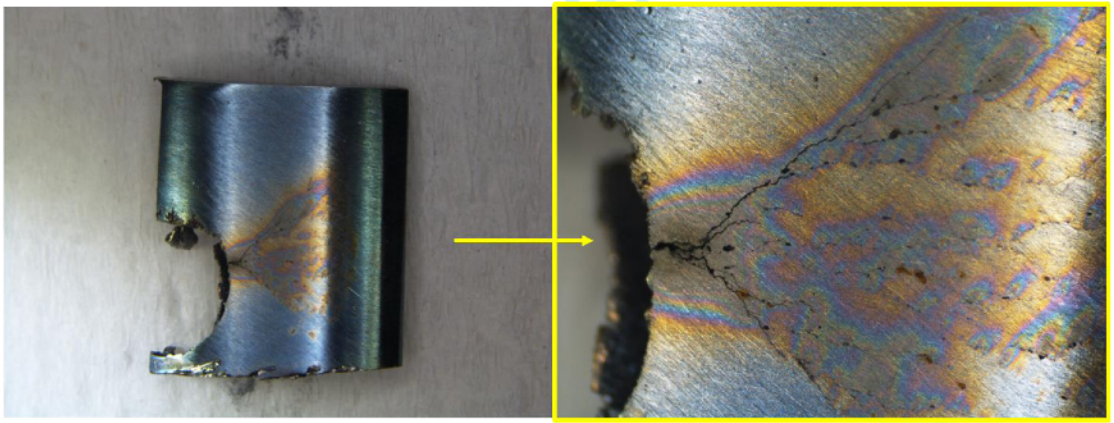

b) As-printed LPBF SS316L, 90% AYS, boiling solution

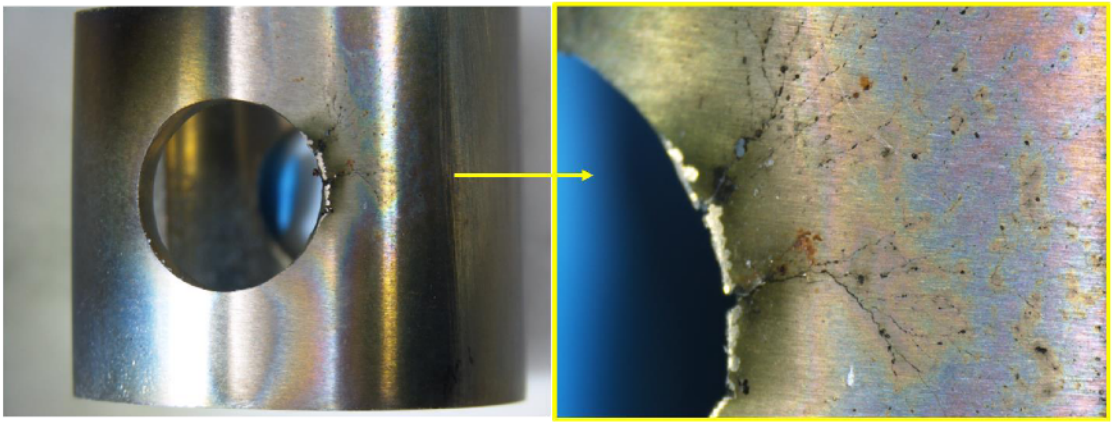

FIGURE 6. a) SCC in the as-printed LPBF SS316L unstressed C-ring when tested in boiling solution, and b) SCC in the as-printed LPBF SS316L C-ring tested in boiling solution while stressed at 90% AYS.

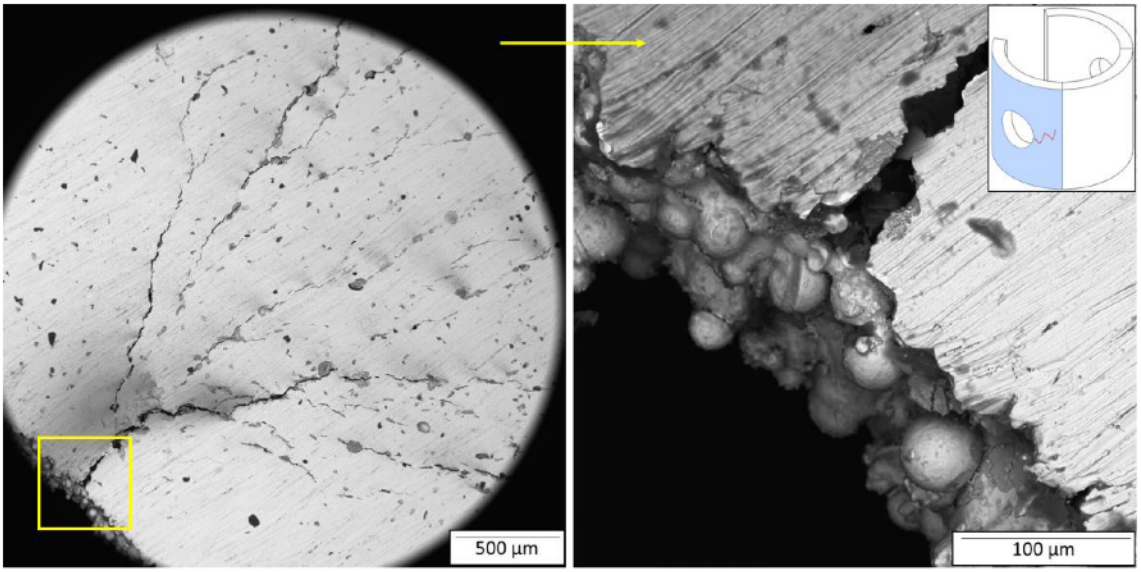

FIGURE 7. FE-SEM image showing SCC in unstressed as-printed LPBF SS316L C-ring that initiated from its printed hole and propagated perpendicular to the print direction. The highlighted blue region in the depicted C-ring shows the location of the crack.

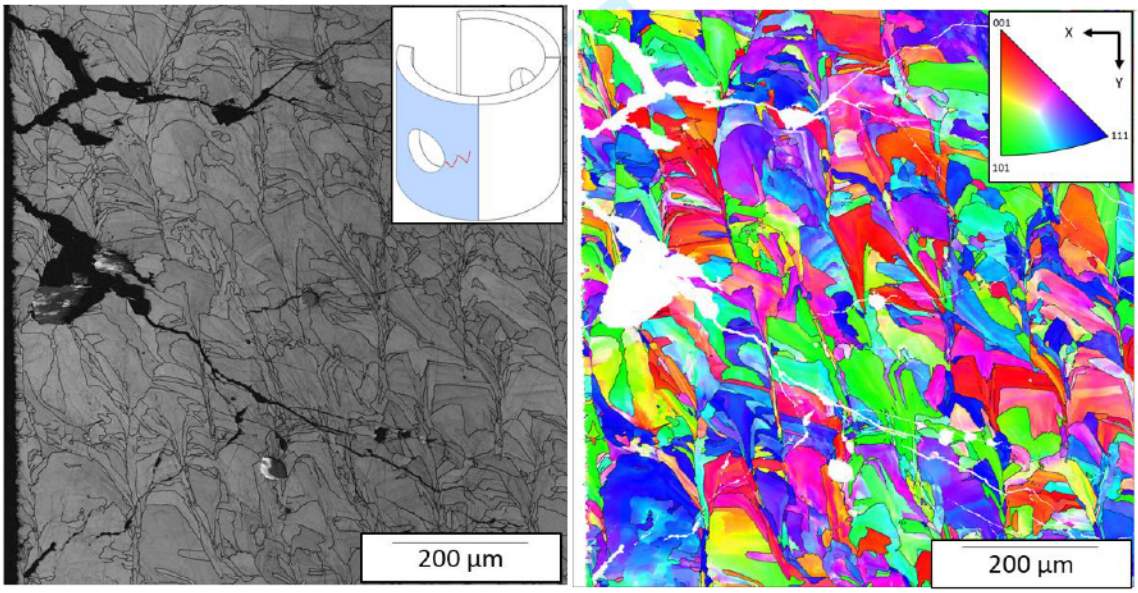

FIGURE 8. Band contrast image and corresponding EBSD map of SCC in as-printed unstressed LPBF SS316L C-ring tested in boiling solution. It can be seen that the crack is transgranular. The highlighted blue region in the depicted C-ring shows the location of the crack.

a) LPBF SS316L - As-printed

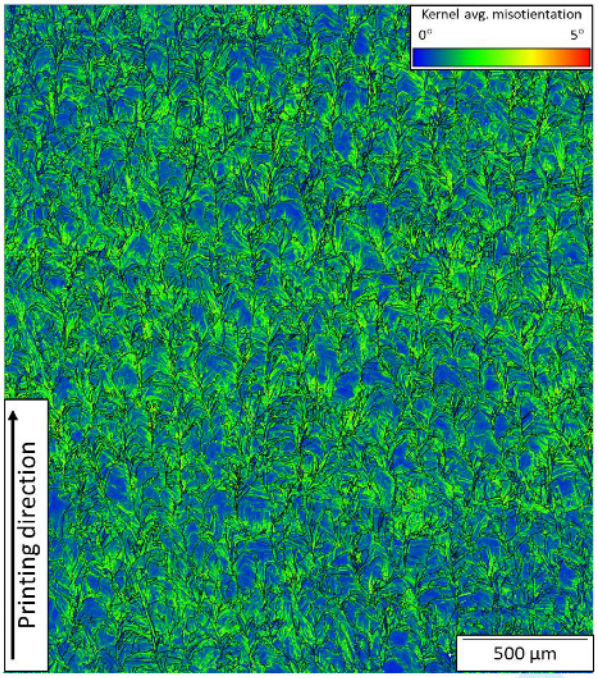

b) LPBF SS316L – Heat treated (650 °C, 2 h)

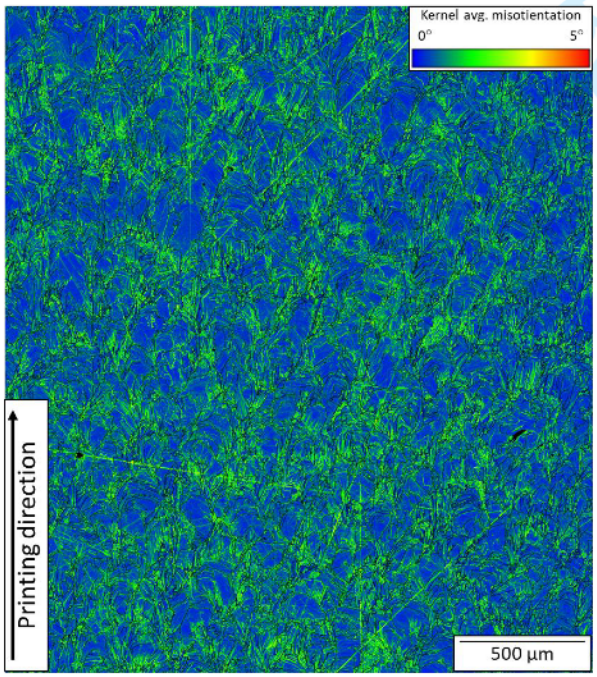

c)

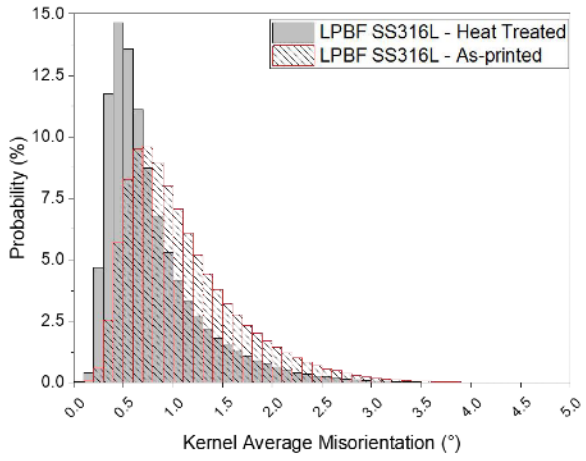

FIGURE 9. a) KAM map of untested as-printed LPBF SS316L C-ring showing a microstructure populated with residual stresses represented by the local plastic deformation depicted by the green areas. b) KAM map of untested heat-treated LPBF SS316L showing a reduction of the residual stresses. c) KAM histogram showing the redistribution of local misorientations after heat treatment of the LBPF SS316L.

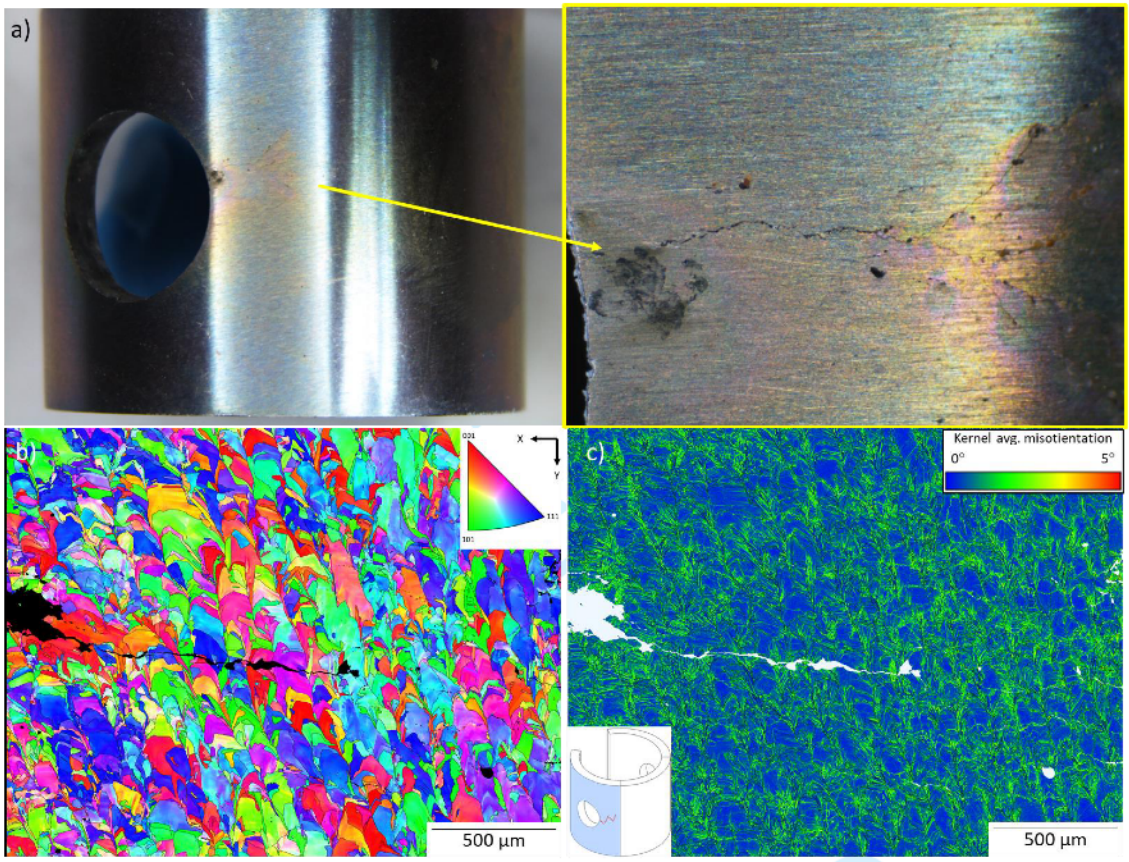

FIGURE 10. SCC in heat-treated LPBF SS316L unstressed C-ring when tested in boiling solution shown in a) photographic image, b) EBSD map and, c) KAMP map.

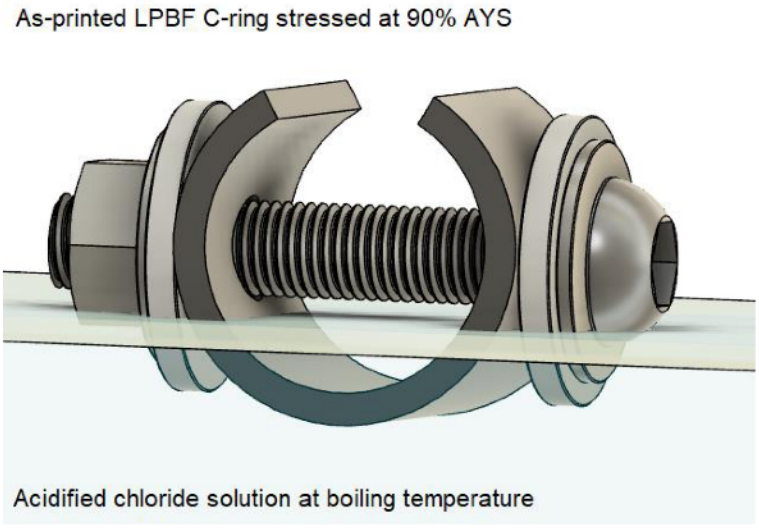

FIGURE 11. Test schematics of the as-printed LPBF SS316L C-ring stressed to 90% AYS and partially immersed in boiling solution.

a) As-printed LPBF SS316L, 90% AYS, boiling solution, partially immersed

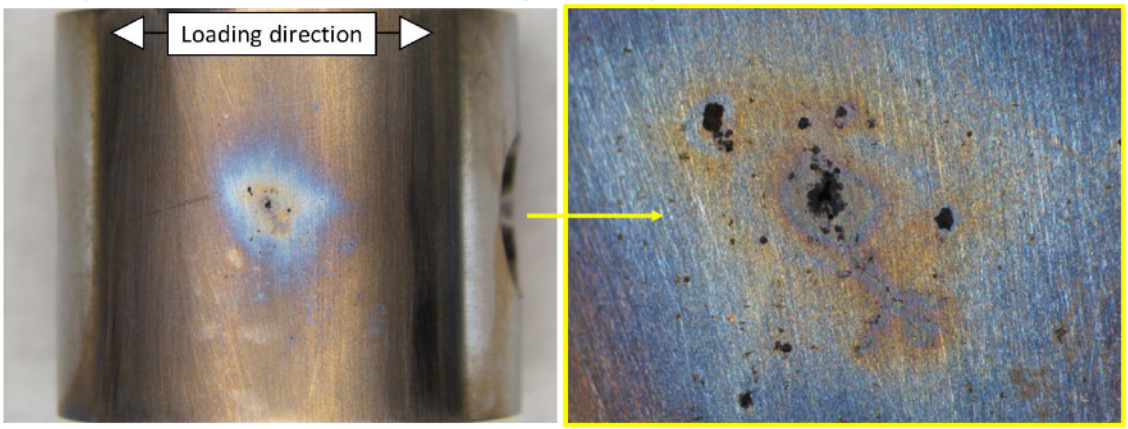

b) Wrought SS316L, 90% AYS, boiling solution

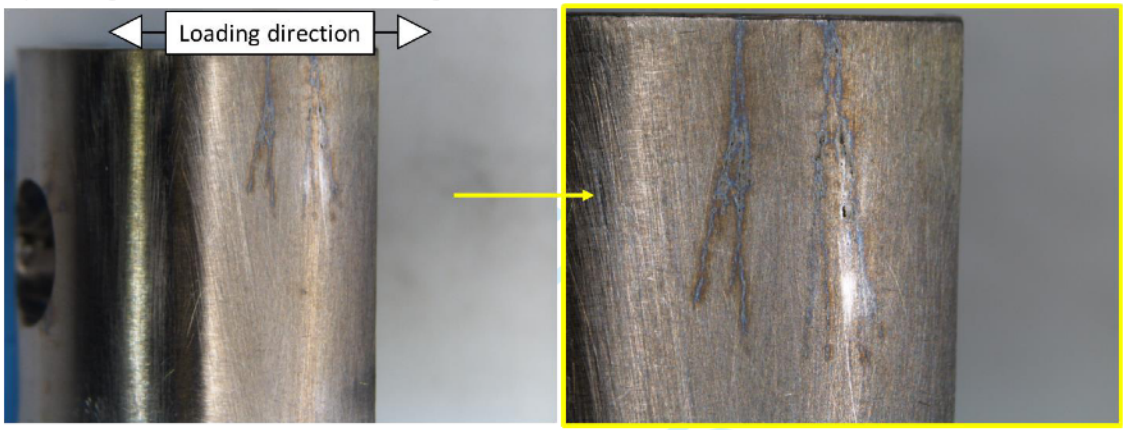

FIGURE 12. C-rings showing SCC at their areas of maximum applied stress, i.e., 90% AYS, when tested in boiling solution. a) As-printed LPBF SS316L partially immersed, and b) wrought SS316L completely immersed.

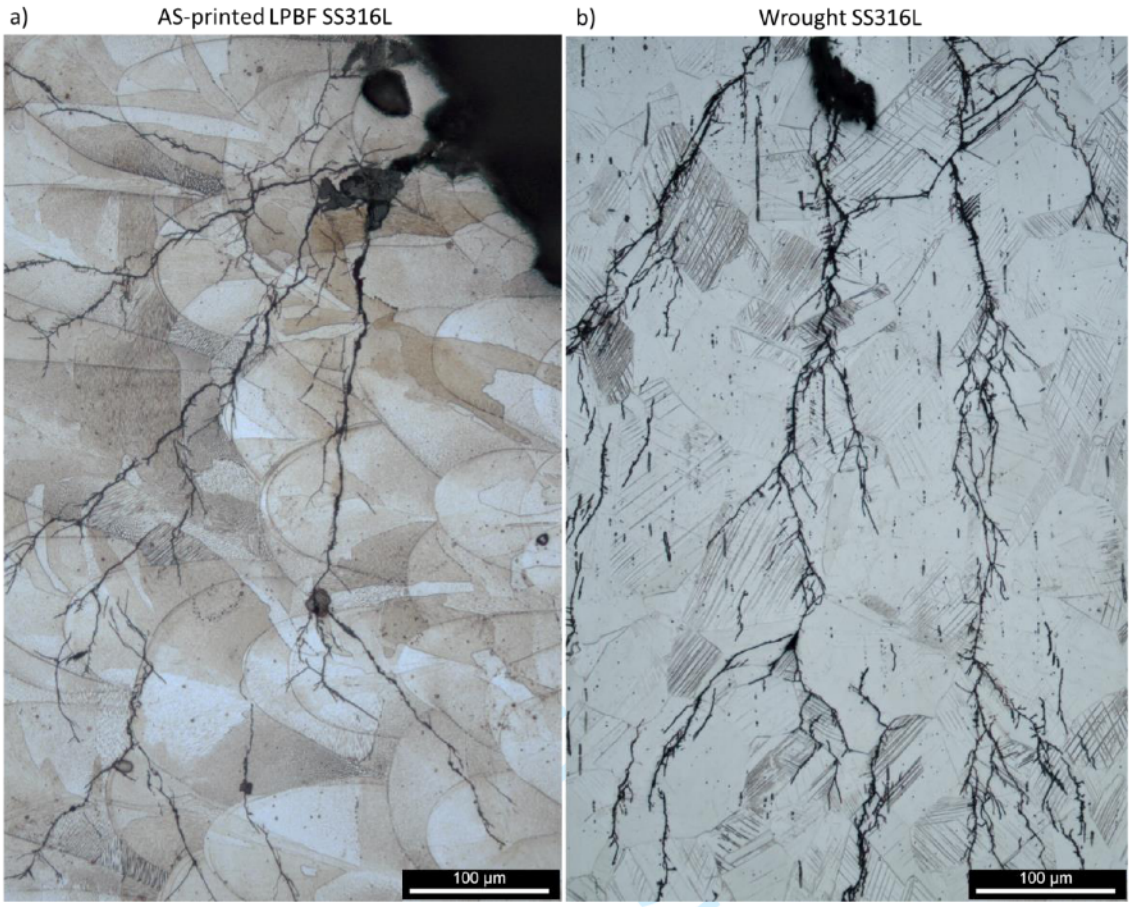

FIGURE 13. Etched microstructures showing transgranular SCC in a) as-printed LPBF SS316L C-rings partially immersed in boiling solution while stressed at 90% AYS, and b) wrought SS316L C-ring fully immersed in boiling solution while stressed at 90% AYS.

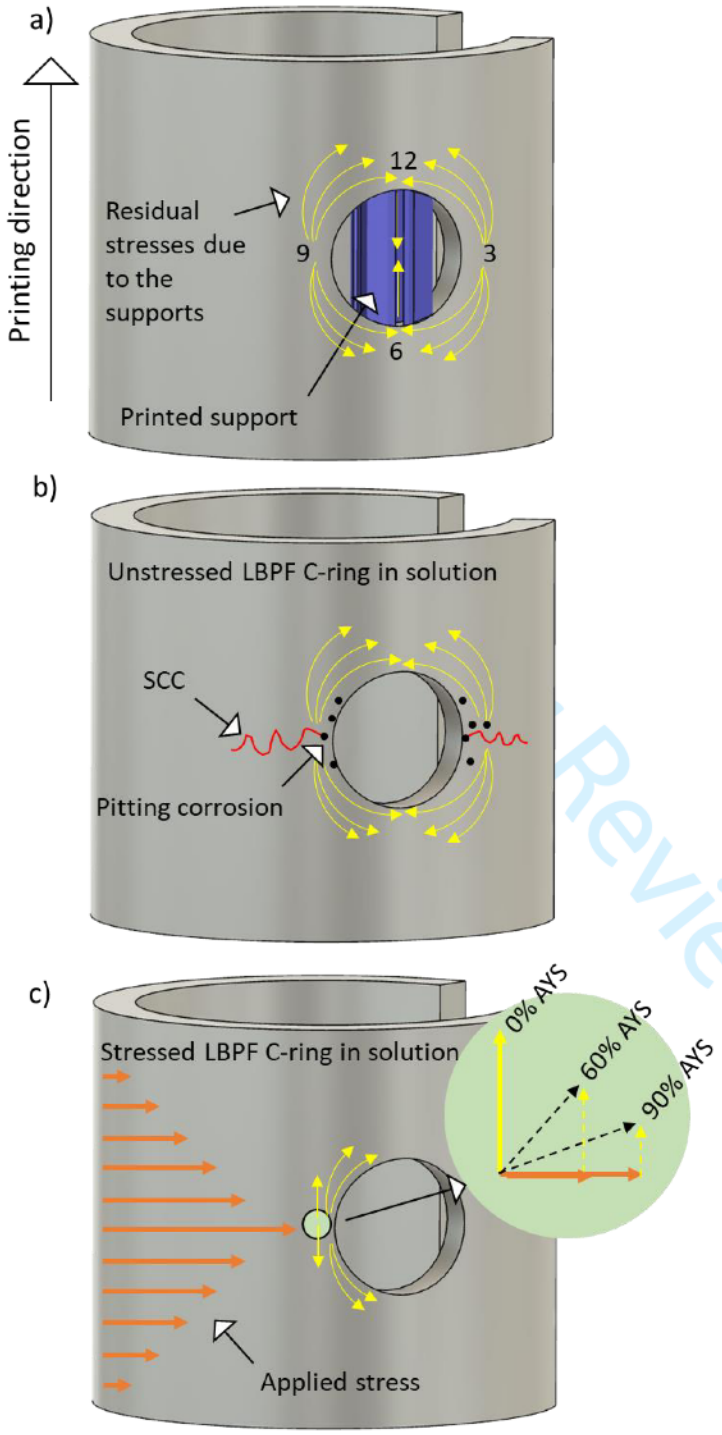

FIGURE 14. a) Depiction of the residual stresses produced in the hole/support interface of the C-rings, b) depiction of an unstressed C-ring with SCC initiating from corrosion pits at the 3 and 9 o'clock sites, and c) depiction of a stressed C-ring and the "relieving" effect of the applied load over the residual stresses.